



Supplement of

Understanding greenhouse gas (GHG) column concentrations in Munich using the Weather Research and Forecasting (WRF) model

Xinxu Zhao et al.

Correspondence to: Jia Chen (jia.chen@tum.de)

The copyright of individual parts of the supplement might differ from the article licence.

Supporting Information

S1 Additional information about the inputs of our modelling framework

The geographical input used for the three domains of our model is obtained from the modified International Geosphere-Biosphere Programme global land cover classification, and relies on data from the Moderate Resolution Imaging Spectroradiometer (IGBP-Modified MODIS; Friedl et al. (2010)). The resulting IGBP-Modified MODIS database has a resolution of 5 30 arc seconds (approximately 1 km) and can provide 20 land-cover categories that are mainly related to different types of vegetation (e.g., evergreen forest, mixed forest). However, the IGBP-Modified MODIS database, as well as other common geographical databases, has only one land-use category defined for urban areas.

The meteorological initial conditions and lateral boundary conditions are obtained from ERA5, the fifth-generation reanalysis produced by the European Center for Medium-Range Weather Forecasts (ECMWF). In ERA5, a variety of observations 10 from more than 20 satellites, radiosondes, aircraft measurements, etc. have been combined and assimilated (Hersbach et al., 2020). ERA5 provides hourly meteorological fields with a horizontal resolution of 31 km and 137 vertical model levels from the surface up to 0.01 hPa (as available via the Copernicus Climate Change Service, <https://www.ecmwf.int/en/forecasts/datasets/reanalysis-datasets/era5>).

The initial and lateral boundary conditions for our simulated concentration fields are from experiment ‘gznv’ of the Integrated 15 Forecasting System (IFS) Cycle 45r1. This simulation has been implemented by ECMWF and is a key part of the Copernicus Atmosphere Monitoring Service (CAMS, as available via Atmosphere Monitoring Service, <https://confluence.ecmwf.int/pages/viewpage.action?pageId=116963341>). The IFS Cycle 45r1 provides 6-hourly estimated mixing ratios of CO₂ and CH₄ with a horizontal resolution of approximately 40 km (following the N256 reduced Gaussian grids from ECMWF) and a vertical resolution of 137 levels (Browne et al., 2019; Rémy et al., 2019).

20 S2 Improved VPRM

As mentioned in Sect. 2, the CGLS-LC100 land cover map has been used to refine the vegetation classification over the innermost domain. Figure 2 shows the refined map of the domain using CGLS-LC100 (left), the original map classified with SYNMAP (middle) and the difference between the two maps (right). As seen in the middle plot, the original map shows no 25 vegetation type classified in the middle of the domain, i.e., the city of Munich. After our refinement, more vegetation types can be recognized inside the city of Munich. Table S1 shows the details on how the Copernicus classes were reclassified into the eight vegetation fraction classes used in the VPRM preprocessor.

S3 EU Local Climate Zones (LCZ) map

The EU LCZ map used in our study was generated with the protocol supported by the World Urban Database and Access Portal Tools project (WUDAPT, as available via <http://www.wudapt.org/>). The LCZ classifications are used for distinguishing different types of landscapes, which include ten land-cover types defined for urban areas (e.g., compact high-rise, compact low-rise), and another seven land-cover types for vegetation types that are not used in our model. The LCZ classification is illustrated in Fig. 1 of Demuzere et al. (2019). In terms of WUDAPT, the morphological urban features are captured within multi-spectral images from satellites (e.g., Landsat 8). Moreover, the LCZ types for the targeted area are identified by a random forest classifier (See et al., 2015). For our study, we extracted the area of our innermost domain from the full EU LCZ map (Demuzere et al., 2019). Then the morphological information from this clipped LCZ map was extracted and transformed into the format used in the WRF pre-processor (Brousse et al., 2016).

As shown in Fig. S1, there are in total 9 LULC categories that cannot be classified over D03 and are marked in red on the X-axis. Furthermore, these extraneous categories are removed from the legend of Fig. 1.

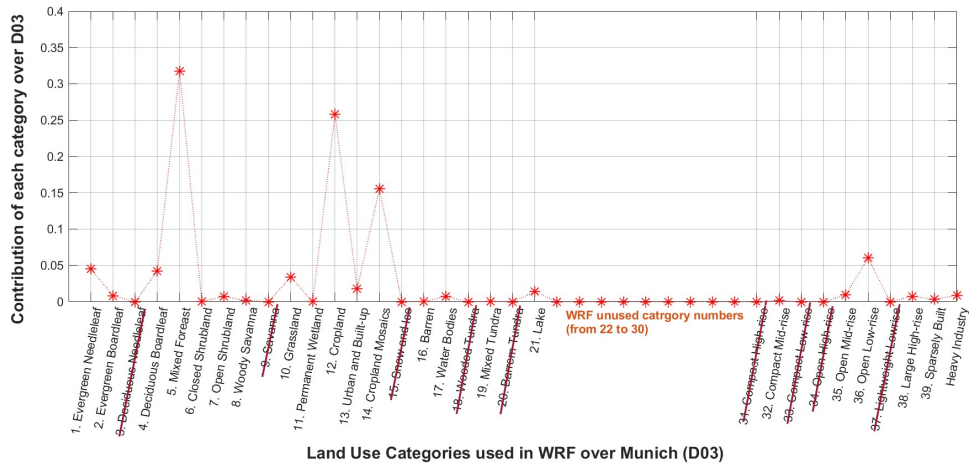


Figure S1. The contribution of each land use land cover (LULC) category over Munich (D03). The categories marked by red lines on the X-axis represent the absence of such LULC categories on D03.

40 S4 Relevant information regarding TNO_GHGco_v1.1

S4.1 Vertical emission profiles for point sources

The vertical emission profiles for point sources we use in this study are provided by Bieser et al. (2011). We re-allocated the layers in this vertical emission profiles (see Fig. S2(a)) to the model layers of of model. The re-allocated vertical profiles for point sources are shown in Fig. S2(b).

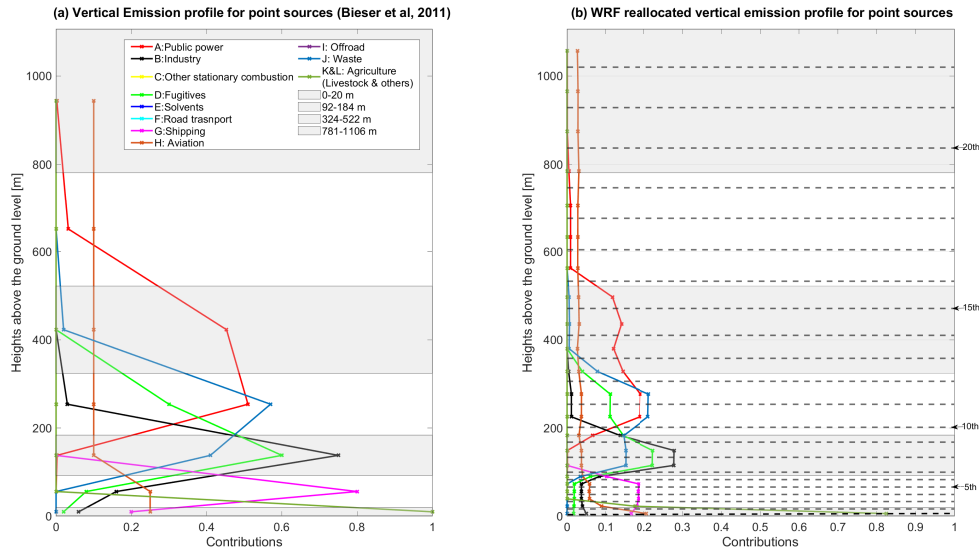


Figure S2. Vertical emission profiles for point sources (a) from Bieser et al. (2011) are re-allocated to our WRF vertical layers (b). The alternating gray and white background stands for the seven vertical layers used by Bieser et al. (2011). The dashed lines in (b) delimit the first 22 vertical layers above the ground in our WRF setup.

45 S4.2 Reclassification of the GNFR categories in TNO_GHGco_v1.1

As described in Sect. 2 of the main text, TNO_GHGco_v1.1 follows the GNFR sector classifications (Super et al., 2020). We aggregate eleven emission sectors from GNFR (see the categories in the legend of Fig. S2) to five major sectors applied in different tracers of our model. The details on the aggregation are shown in Table S2 for CO₂ and Table S3 for CH₄.

S5 Comparisons of other meteorological variables

50 Expanding on Sect. 3.1 of the main text, here we discuss plots comparing our model wind fields to DWD measurements and our modelled temperature and precipitation to measurements from LMU and DWD.

Table S2. Aggregation of emission categories for CO₂ from GNRF to our model.

GNFR	Categories in WRF for CO ₂				
	A. Power Plants	B. Industry	C. Other Stationary Combustion	D. Road Transport	E. Others
A:Public power					
B:Industry					
C:Other stationary combustion					
D:Fugitives					
E:Solvents					
F:Road transport					
G:Shipping					
H:Aviation					
I:Offroad					
J:Waste					
K&L: Agriculture (Livestock & others)					

Table S3. Aggregation of emission categories for CH₄ from GNRF to our model.

GNFR	Categories in WRF for CH ₄					
	A. Power Plants	B. Industry	C. Agriculture	D. Waste Management	E. Fugitives and solvents	F. Others
A:Public power						
B:Industry						
C:Other stationary combustion						
D:Fugitives						
E:Solvents						
F:Road transport						
G:Shipping						
H:Aviation						
I:Offroad						
J:Waste						
K&L: Agriculture (Livestock & others)						

S5.1 Wind comparison between the model and the DWD Munich Airport station

Figure S3 shows a comparison between the modelled and the measured values obtained from the DWD Munich Airport station (see Sect. 3 of the main text, where also Figure 2 showed the measurements of the LMU station). As depicted in the wind roses of Fig. S3(a), the prevailing measured surface wind blows from the southwest, while the modelled directions show more variations. Mismatches of wind directions mainly appear during daytime, but the overall trends can be reproduced by the model (red crosses in Fig. S3(c); RMSE: 72 ° and MAE: 17.83 °). In terms of wind speeds (see Fig. S3(b)), the model matches well with the measurements with a RMSE of 1.58 m/s and a MAE of 0.15 m/s. At nighttime, the measurement exhibits higher wind speeds under the same wind directions, compared to the model (see Fig. S3(a.5) & (a.6)).

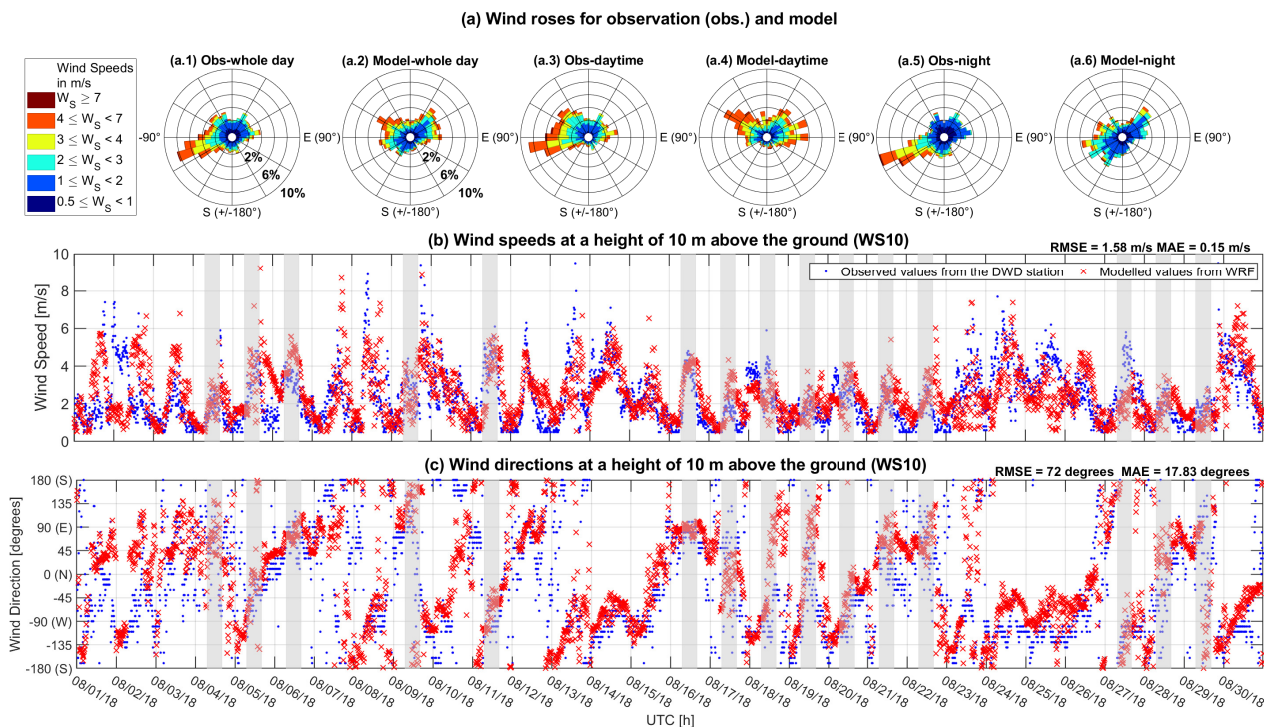


Figure S3. Wind roses (a) and time series of simulated and observed wind speeds (b) and wind directions (c) at a height of 10 m above the ground at Munich Airport (DWD station). Wind roses for the measurements over August 2018 are plotted in Panels (a.1): 24 hours, (a.3): daytime from 6 am to 5 pm only, and (a.5): nighttime only, while Panels (a.2), (a.4), and (a.6) represent the modelled values. Each wind rose indicates WS10, WD10 and the frequency (% scale) of wind coming from a particular direction during the targeted period. The blue dots in Panels (b) & (c) represent the measured values from the DWD station and the red crosses represent the simulation. The grey shaded areas mark the measurement periods used for the model-measurement comparison of column concentrations in Sect. 4 of the main text.

60 S5.2 Comparisons of other meteorological variables

Apart from the wind fields mentioned above, other meteorological parameters are also expected to impact the behavior of the tracers in our model. The temperature at a height of two meters above the ground (T2) plays a key role in calculating biogenic fluxes in VPRM (Mahadevan et al., 2008). Precipitation is also an important point in assessing the model behavior, since the functionality of our instrument used for measuring the column concentrations is influenced by rainfall, as described in detail in

65 Sect. 4.1.

Figure S4 compares T2 and precipitation between models and measurements. Over the entire simulation period, the modelled T2 (red lines in Fig. S4(a) & (b)) shows trends similar to the measurements (black and blue lines) from both weather stations. As illustrated in Fig. S4(b), a better agreement appears to exist between the model and values from the LMU station, with a RMSE of 2.1 K and a MAE of -0.23 K, while the RMSE between the simulated values and those measured at DWD is 2.3 K,

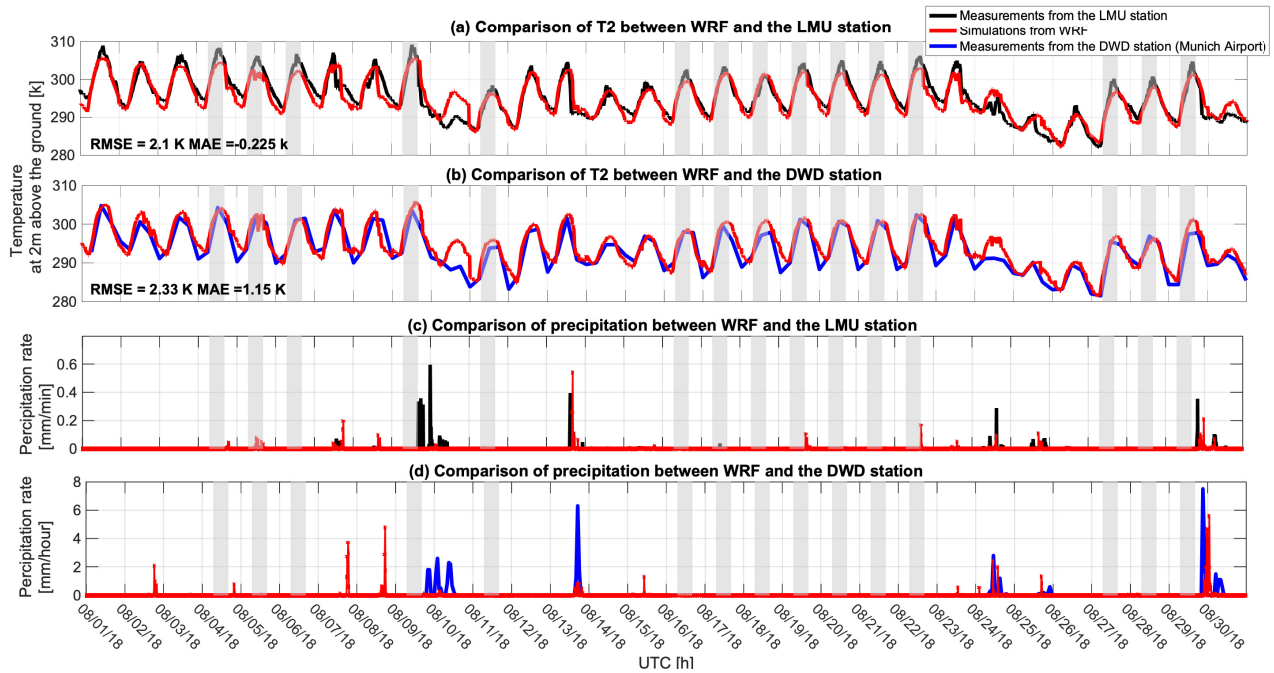


Figure S4. Comparison of temperatures at a height of 2 meters above the ground (T2; upper two panels) and precipitation values (lower two panels) between the model and two stations from 1 to 30 August, 2018: Panels (a) & (c) display data from DWD and Panels (b) & (d) show values from the LMU station. In all subplots, the simulations are plotted using the red lines while the measurements from the LMU and DWD stations are represented by the black and blue lines, respectively. The grey shaded areas mark the measurement periods used for comparing to the simulations in Sect. 4.

70 and the simulated values are generally higher (MAE: 1.15 K). During the daytime, the curves of the modelled and measured T2 generally match well, apart from the appearance of some peaks at noon measured by the LMU weather station (Fig. S4(b)). Major discrepancies of T2 between models and measurements occur during nighttime, at the early morning and at specific days, e.g., 10 and 24 August.

One of the potential reasons for the discrepancies between models and measurements on these two specific days is that 75 the mesoscale model can not reproduce the precipitation on these two days well, especially for 10 August. The missing or weak precipitation potentially led to unrealistic temperatures. As evident in Fig. S4((c) & (d)), most of the rainfalls in August, 2018 can be replicated by the model, but the magnitude of the precipitation is not always well estimated. The disagreement in precipitation between the model and measurements can be due to several potential error sources. For instance, the spatial resolution of the mesoscale model may be not sufficient to fully reproduce complex flow features on the micro-scale or to 80 resolve orographic uplift, but these effects can have an impact on the measurements (Collier et al., 2013).

S6 Measurement days – data-quality characteristics

Some characteristics pertaining to the quality of the data obtained on our measurement days from 1 to 30, August in 2018 (which motivate further study of particular days) are illustrated in Table S4 below. The criteria for the assessment in the table are based on studies for the Berlin region (Hase et al. 2015; cf. their Table 1) and for Paris (Vogel et al. 2019; cf. their Table 2).

85 As a basic prerequisite, all the measurement sites should work, otherwise the overall quality is set to be '+'. The overall quality levels are then determined from the observational coverage during one day: daily temporal coverage lower than 25 %: '+'; from 25 % to 50 %: '++'; from 50 % to 75 %: '+++'; from 75 % to 100 %: '++++'. The observational coverage at more than three sites has to satisfy the criterion.

S7 Comparison between the model and the measurements for the rest of the selected dates

90 Figures S5 and S6 show the modelled and measured column concentrations of CO₂ and CH₄, with contributions from different tracers for the rest of the selected dates, complementary to figures 5 and 6 of the main text.

S8 The map of the modelled Net Ecosystem Exchange (NEE)

The maps of the modelled net ecosystem exchange (NEE) for the outermost domain on a sample date (21 August) are plotted in Fig. S7. The southern part of the EU is more biologically active and has greater carbon sinks compared to more northerly
95 regions. As a result, sometimes air masses from the northern part of the EU mix with air masses with less CO₂ (due to the biospheric uptake) from the southern part of the EU near to the Alps, close to Munich and the center of our domain.

S9 Wind roses during the daytime

Figure S9 provides the daytime wind roses (from 6:00 UTC to 17:00 UTC) day by day from 1 to 30 August, 2018. Each wind rose shows wind speeds and wind directions at 30 meters above the ground at LMU.

100 S10 Comparison of pressure and temperature profiles between the model and the values from the instruments

For the five instruments deployed in MUCCnet, one pressure profile is used for the measurement retrieval. The WRF model provided pressure and temperature at a much finer spatial resolution than that of NCEP, at a horizontal resolution of 400 m and with 45 vertical levels. To investigate whether discrepancies of pressure between the values used in the retrieval and the WRF model values could have a significant impact, we extracted the pressure and temperature profiles from the ".map" file
105 used in the retrieval. Figure S10 shows the comparison between these retrieval values and the modelled values. In general, only small difference in temperature and pressure are found above around 10 km. As the modelled pressure profiles match the

Table S4. Summary of day-by-day main characteristics of measurement days from 1 to 30, August in 2018 at our five measurement sites, including the number of measurement points for each site, overall data coverage for each measurement date (with the classifications from poor to excellent: +, ++, +++, +++) based on the available observations, averaged wind speeds during the day time, and wind directions at the ground level obtained from the LMU stations (Hase et al., 2015; Vogel et al., 2019)

Date	Quality	Number of Observations					Wind Speed	Wind Direction
		Garching (North)	TUM (Center)	Höhenkirchen (South)	Markt Schwaben (East)	Weßling (West)		
20180801 (Wed)	+	15	127	0	0	0	2.56	W-N-E
20180802 (Thu)	+	0	131	0	0	35	2.92	W-N-E
20180803 (Fri)	+	28	137	82	0	50	2.70	W-N-E
20180804 (Sat)	++++	127	131	125	125	60	2.11	N-E
20180805 (Sun)	++++	110	131	82	99	68	2.83	NW-NE
20180806 (Mon)	+++	114	126	124	126	88	3.19	NE
20180807 (Tue)	+	0	47	0	53	23	2.10	W-N-SE
20180808 (Wed)	++	89	92	76	106	37	3.30	W-N
20180809 (Thu)	++++	112	97	106	106	130	2.49	SE-N
20180810 (Fri)	+	0	0	0	0	0	2.19	N-W-S
20180811 (Sat)	+++	100	93	91	114	99	3.29	W
20180812 (Sun)	+	130	0	135	135	136	2.68	E-N
20180813 (Mon)	+	73	81	72	93	68	3.10	W-N-W
20180814 (Tue)	+	0	0	0	0	0	3.16	NW
20180815 (Wed)	+	57	94	0	89	46	2.26	SW-N-NE
20180816 (Thu)	++++	110	133	105	133	133	2.97	E-NE
20180817 (Fri)	+++	102	130	131	132	97	1.87	W-N-E
20180818 (Sat)	+++	75	69	100	98	71	2.56	NW
20180819 (Sun)	++++	127	130	129	132	127	2.03	W-N
20180820 (Mon)	++++	126	127	126	131	112	2.25	W-N
20180821 (Tue)	+++	109	131	115	130	109	2.44	NW-N-E
20180822 (Wed)	++++	129	130	128	130	129	2.26	N-E
20180823 (Thu)	++	60	102	75	72	72	3.14	W-N-S
20180824 (Fri)	+	0	0	0	0	0	3.79	W
20180825 (Sat)	+	0	0	0	0	0	3.16	W
20180826 (Sun)	+	23	83	28	0	0	2.28	W-N-E
20180827 (Mon)	+++	81	75	98	101	61	2.95	W
20180828 (Tue)	+++	66	72	104	99	75	2.18	NE
20180829 (Wed)	+++	79	86	55	86	94	1.71	SW-N-E
20180830 (Thu)	+	0	0	0	0	0	2.52	W

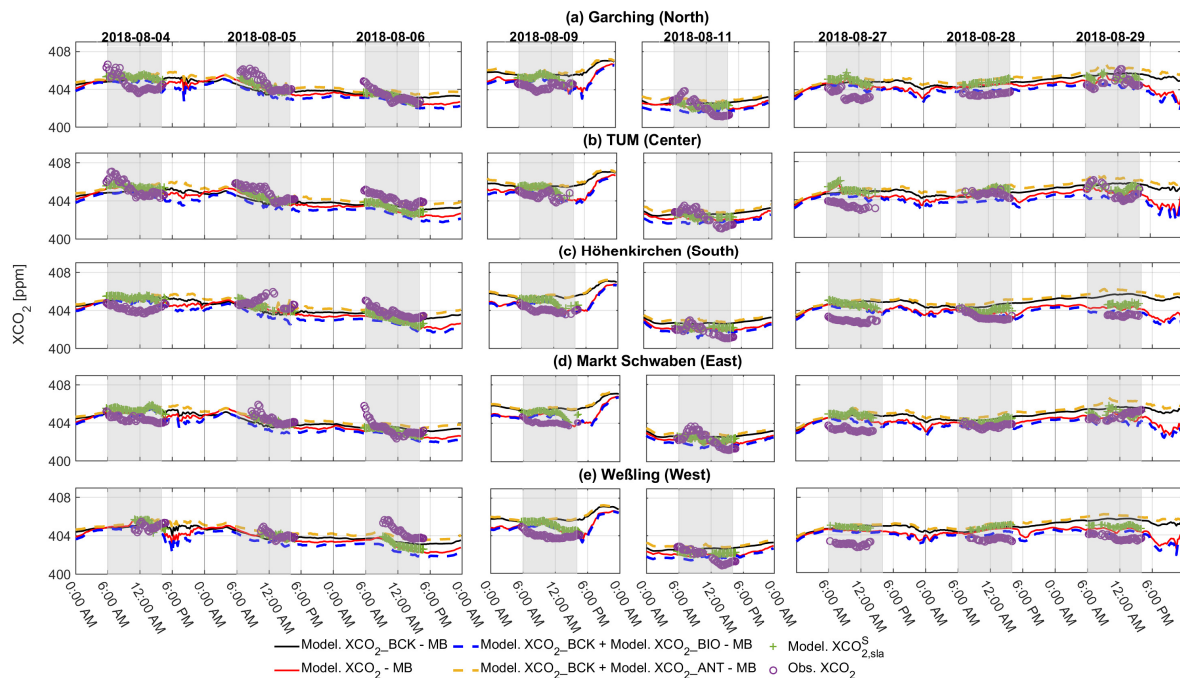


Figure S5. Modelled $XCO_{2,sla}^S$, attribution of variations to different tracers, and the measurements at five sites of MUCCnet for the dates studied but not shown in Fig. 5 of the main text. The purple circles represent the column measurements from MUCCnet and the green '+' markers stands for the modelled $XCO_{2,sla}^S$ after subtracting the MB. The other lines in the plot give pressure-weighted modelled column concentrations along the full time series. These are calculated following Eq. 1 of the main text (i.e. without smoothing using the SZA-dependent AK) and all corrected by MB. The black curve represents the modelled background XCO_{2_BCK} , and the red curve shows the modelled XCO_2 . The dashed yellow and blue curves highlight the concentration changes caused by human activities (XCO_{2_ANT}) and biogenic activities (XCO_{2_BIO}). The grey shaded areas mark the measurement periods used for comparing observations to model results.

vertical structure of the modelled concentration fields, the modelled column concentrations can be calculated without the need for interpolation.

S11 Discussion of WRF-Chem and STILT

110 Generally, WRF-Chem and STILT are two different types of models and are rather complementary than comparable. WRF-Chem is an Eulerian model, which combines weather prediction with tracer transport and can reproduce or predict high-resolution meteorological and concentration fields on a three-dimensional grid as a frame of reference. STILT, in contrast, is a stochastic Lagrangian (moving frame of reference) model simulating transport with pre-computed (assimilated) meteorological fields as input, whose calculations are offline and computationally efficient. Lagrangian models are efficient also because they
 115 need only resolve the meteorology along the course of a given advected air parcel. The two models are linked in this study

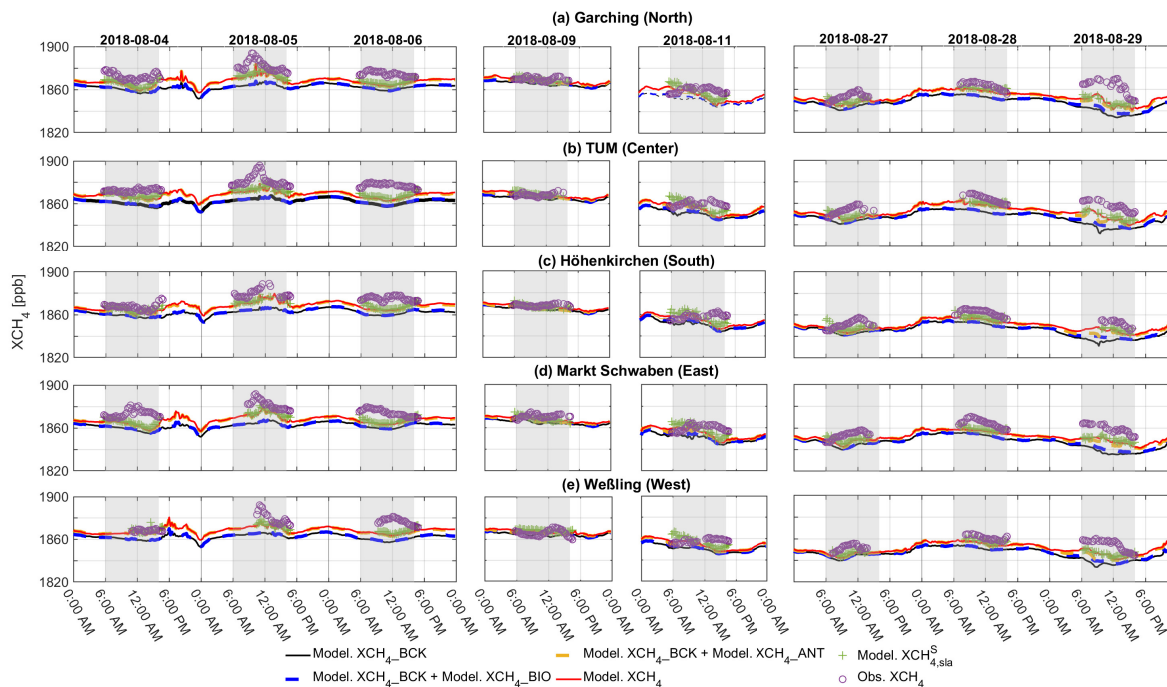


Figure S6. Modelled $XCH_{4,sla}^S$, attribution of variations to different tracers and the measurements at five sites of the MUCCnet for the dates studied but not shown in Fig. 6 of the main text. The purple ‘o’ represents the column measurements from MUCCnet and the green ‘+’ stands for the modelled $XCH_{4,sla}^S$. The other curves in the plot show the modelled column concentrations calculated following Eq. 1 of the main text, i.e. without smoothing using the SZA-dependent AK: black curve – modelled background (XCH_{4_BCK}); red curve – modelled XCH_4 . The dashed yellow and blue curves highlight the concentration changes caused by human activities (XCH_{4_ANT}) and biogenic activities (XCH_{4_BIO}). The grey shaded areas mark the measurement periods used for comparing to the simulations.

because the meteorological output of WRF-Chem is used to drive the particle transport model STILT. Thus, STILT is simply used to derive the footprints, or areas of influence, of the measurements, using the same meteorological fields.

While the ‘direct’ extraction of footprints from WRF outputs is theoretically possible with the adjoint form of WRF, it is considerably more costly and complicated. While there are some differences regarding the representation in the vertical transport between WRF and STILT, we believe that any inconsistencies are irrelevant for the conclusions of this study. Therefore, using STILT driven by WRF meteorology for the purpose of this study is simply an efficient approach. Based on our model-measurement comparison of meteorological fields, particularly winds, we believe that the modelled wind fields from WRF are adequate for both Eulerian and Lagrangian.

Two tables are listed as follows, one for the comparison between the two models with respect to their features, benefits and drawbacks (see Table S5), and another for the basic set-up of the models used in our study (see Table S6).

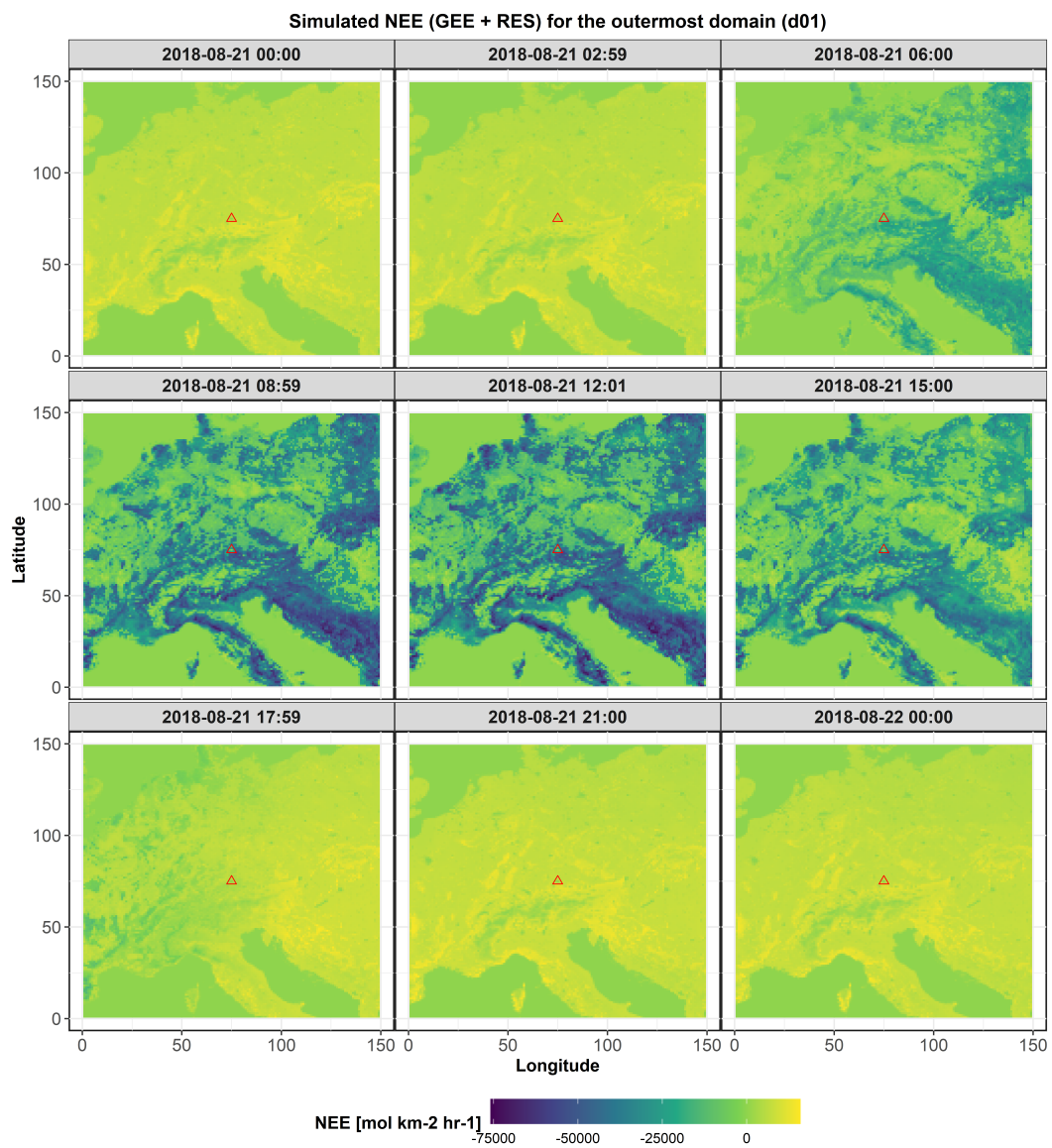


Figure S7. The map of modelled net ecosystem exchange (NEE) on 21 August for the outermost domain (d01).

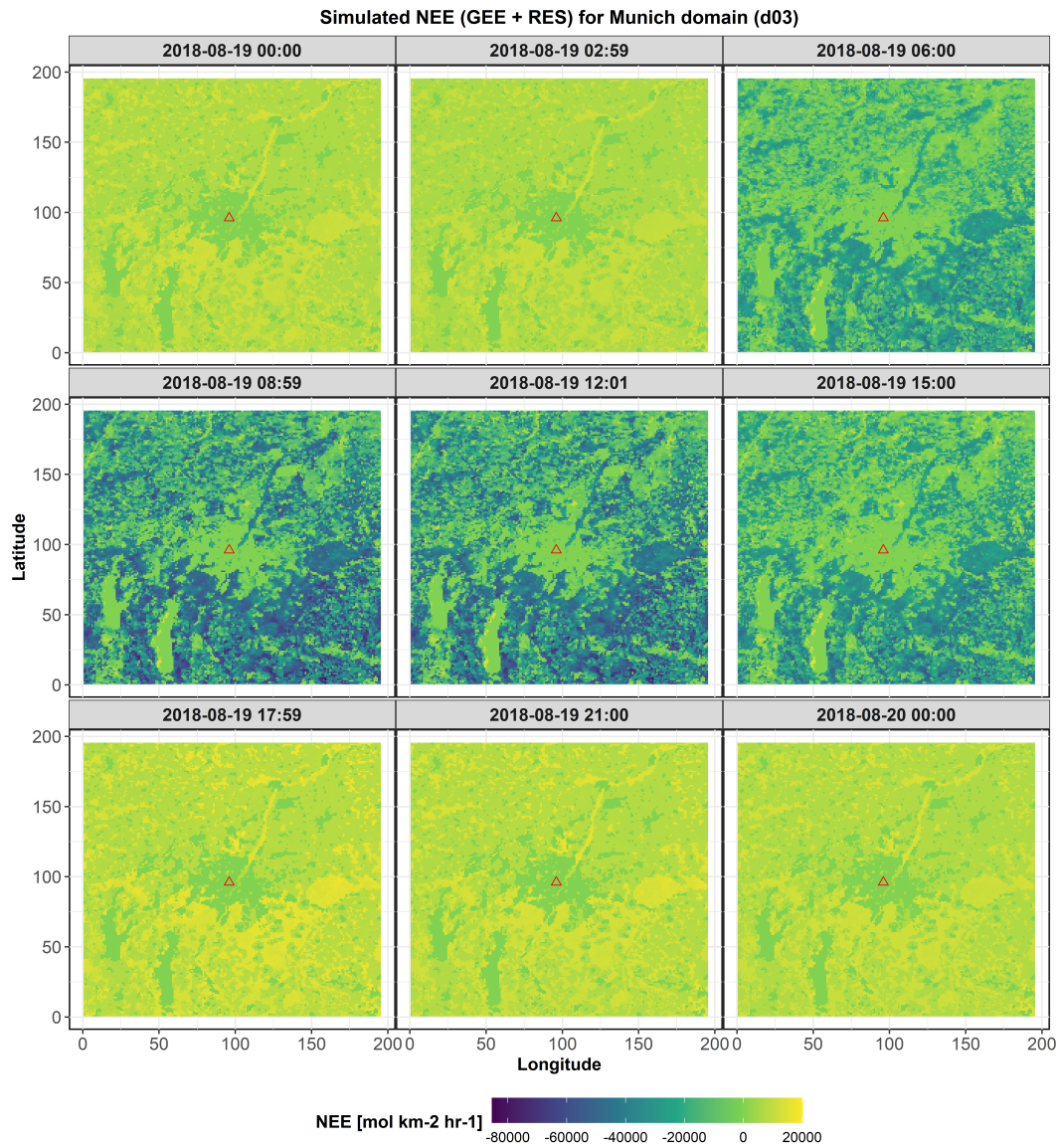


Figure S8. The map of net ecosystem exchange (NEE) on 19 August for the innermost domain (d03), modelled with the VPRM using the new land use categories mentioned in Sect. S2.

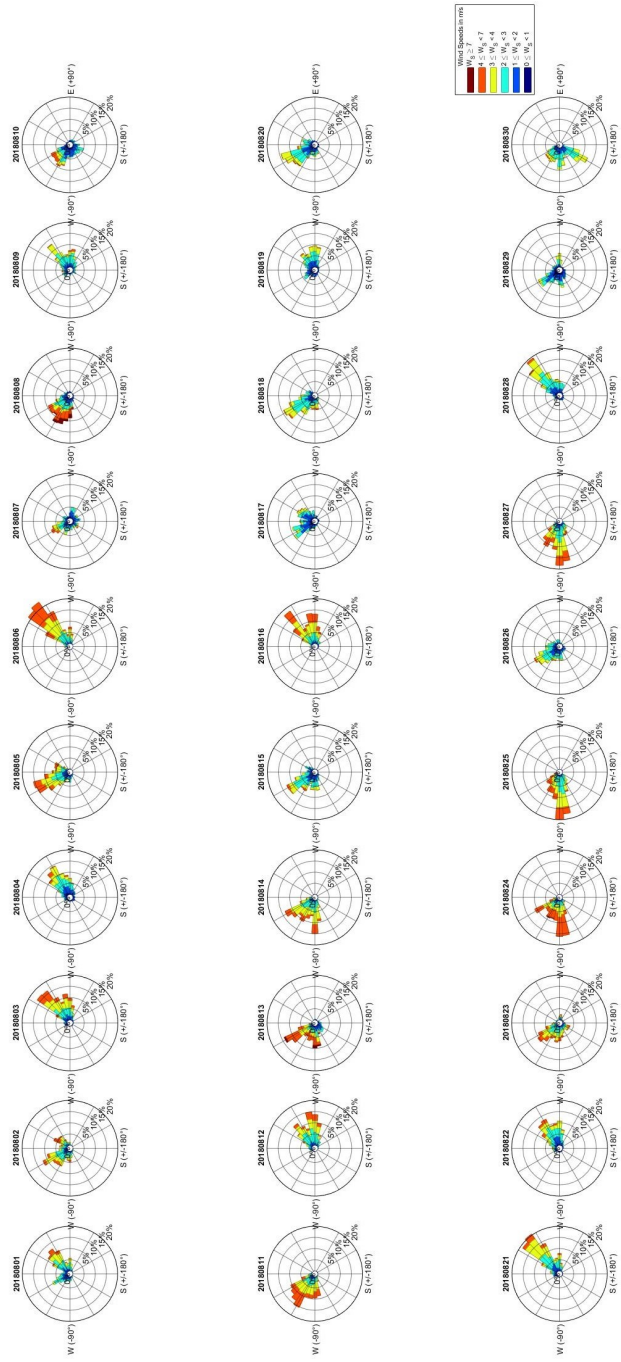


Figure S9. Daytime wind roses, measured day by day at LMU.

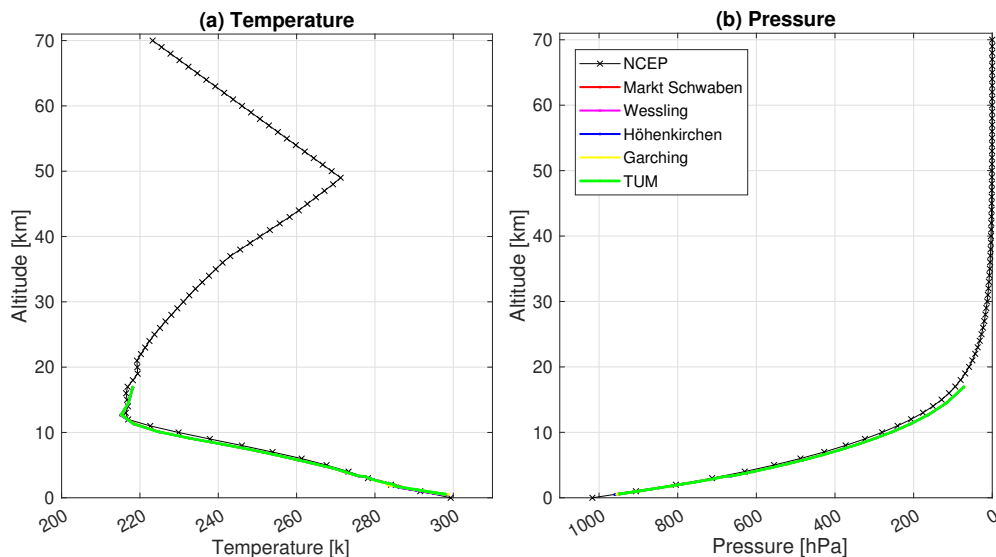


Figure S10. Comparisons of (a) Temperature and (b) Pressure Profiles between the values from NCEP and the WRF modelled values for five MUCCnet sites at 12:00 UTC of 16 August. The profiles of the MUCCnet sites coincide such that only the TUM profile (green graph) remains visible in each panel.

S12 Definition of footprint percentile contours

To define the percentile contours of STILT footprints used in our study, we performed the following steps: first, the values of the slant column footprint map were ordered and the cumulative sum of these sorted values was calculated (see Fig. S11.(a)); Secondly, based on the plot of the cumulative sum of the sorted values, a threshold under a specific percentile was defined to exclude points with lower sensitivity, e.g., the 90th percentile (brown line in Fig. S11.(a)); Finally, the footprint contours of the different percentiles were defined. The generation of footprint percentile contours in our study is based on the approach used in Dayalu et al. (2020).

Table S7 lists the receptor times used for generating the footprint contours in Fig. S11(b) and Fig. 8. As described in Sect. 5, the receptor time (i.e. the time when the air parcels are released from the receptor backwards in time by STILT) is defined based on the observed peak time. In cases where this observed peak time cannot be read from Figs. 5 and 6, it is defined by considering the peak time at a corresponding upwind site and adding a transport time estimate. However, when Höhenkirchen (south) site was to be regarded as a rather upwind site under Northeasterly/Easterly wind, and the peak time is not readable from the figures, its receptor time (see ‘-’ in Table S7).

Figure S12 shows the footprint contours at the up- and downwind sites from 17 to 21 August, 2018. In our study, footprint contours are generated to show the main area travelled by air parcels released from the receptor, which can also be used to understand the prevailing wind conditions over the domain. A footprint contour generated under steady wind conditions always starts at the receptor and spreads gradually in the direction which the air parcels come from. In contrast, unsteady wind

Table S5. Summary of two models used in this study

Name	WRF-Chem (Peckham et al., 2017)	STILT (Fasoli et al., 2018)
Type of Model	Eulerian framework	Lagrangian framework
Background	An extended version of WRF coupled with Chemistry, including aerosol and GHG transport.	An extension of HYSPLIT (The Hybrid Single-Particle Lagrangian Integrated Trajectory) model to simplify atmospheric transport modelling workflows and improve accuracy.
Usage of Model in this study	Simulation of spatial and temporal distributions of tagged trace gases, driven by the WRF modelled meteorology.	Simulation of transport of an ensemble of air parcels at a receptor location backward in time.
Input/Driver	Global reanalysis coarse meteorological databases, gridded emission fluxes and global background concentration profiles.	Global or regional meteorological fields. Vertical profiles of the horizontal and vertical wind components as key drivers.
Mechanism	Dynamical downscaling by solution of differential equations for the meteorological variables with transport/chemistry added using a tracer approach.	Transport of particles is directly followed by using a combination of mean winds from inputs with stochastic fluctuations based on a Markov process (turbulent motions).
Products	Finer meteorological fields and its derivative products, e.g., spatial and temporal distribution of CO ₂ .	Particle trajectories and gridded surface flux footprints (i.e., sensitivities to upstream surface emission fluxes).
Benefits	1. Modelled outputs advanced in both spatial and temporal resolution. 2. Simulation of trace gases simultaneously with the meteorology, without time interpolations. 3. More realistic representation of the atmosphere and numerically more consistent, with the same grid structure of the meteorology. 4. The outputs assessed and used to interpret a variety of types of observations, also from satellites.	1. More computational efficiency and easy extraction of footprints. 2. Concentration enhancements at the receptor which can be obtained by convolving the outputs (footprints) with emission inventories.
Weaknesses	1. High computational requirements. 2. Less flexibility for conducting ensemble modeling and extracting the footprint information.	1. Sensitivity of particle transports to the accuracy of meteorological input fields. 2. Turbulent transport in STILT is reproduced by following a stochastic process (Markov chain), which is highly sensitive to the vertical velocity variance and the Lagrangian time-scale (Pillai et al., 2012).
Relationship	WRF derived meteorological input fields are commonly used to drive STILT.	

Table S6. Basic set-up of two models used in this study

Name	WRF	STILT
Horizontal Resolution	400 m × 400 m	0.01 ° × 0.01 ° (resolution of footprints)
Vertical layers	45	13 (particles' release height)
Meteorological inputs	ERA5 (37 km × 37 km), Emission fluxes from TNO-MACC, background concentration profiles from CAMS.	WRF output from the middle domain (D02; 1 km × 1 km).
Final products	Spatial and temporal distributions of meteorological fields and tagged trace gases (i.e., CO ₂ and CH ₄).	Gridded pressure-weighted column footprints for five MUCNet sites.

results in the disordered travel of air parcels, making it hard to relate the prevailing wind direction to the footprint contours. In the classical DCM, the air masses should theoretically pass by the upwind site and further arrive at the downwind site with a relatively stable wind, after travelling through an urban area in which most of emissions are located. The cause why the other dates are excluded in the discussion is that not all sites for these two days meet the criteria to be selected as either downwind or upwind sites under the wind conditions of that day, based on Table 1 of the main text. As shown in Fig. S12(c), under such a prevailing wind of (i.e., northeasterly), Weßling (West) should be selected as the downwind site for the calculation of concentration gradients. But some part of the upstream at this downwind site did not overlap the upstream of the other three upwind sites, shown in Table 1 of the main text. Specifically, some air does not pass the upwind sites (mainly from the south/southeast region of Munich) and arrives at Weßling together with other airs that pass the upwind sites. This is also the case for 17 and 20 August (see Fig. S12(a) & (d)). In terms of 18 August, under the prevailing winds (northwesterly), the upwind site is supposed to be Weßling (west), while the other three sites should be the downwind sites based on Table 1. But as shown in Fig. S12(b), the in-flowing airs reaching Weßling (red line) are mainly from the northern region of Munich, and could not further pass the other three downwind site.

Using our refined DCM approach discussed in Sect. 5.3 of the main text, we can apply DCM for three dates: 16, 20, and 21 August.

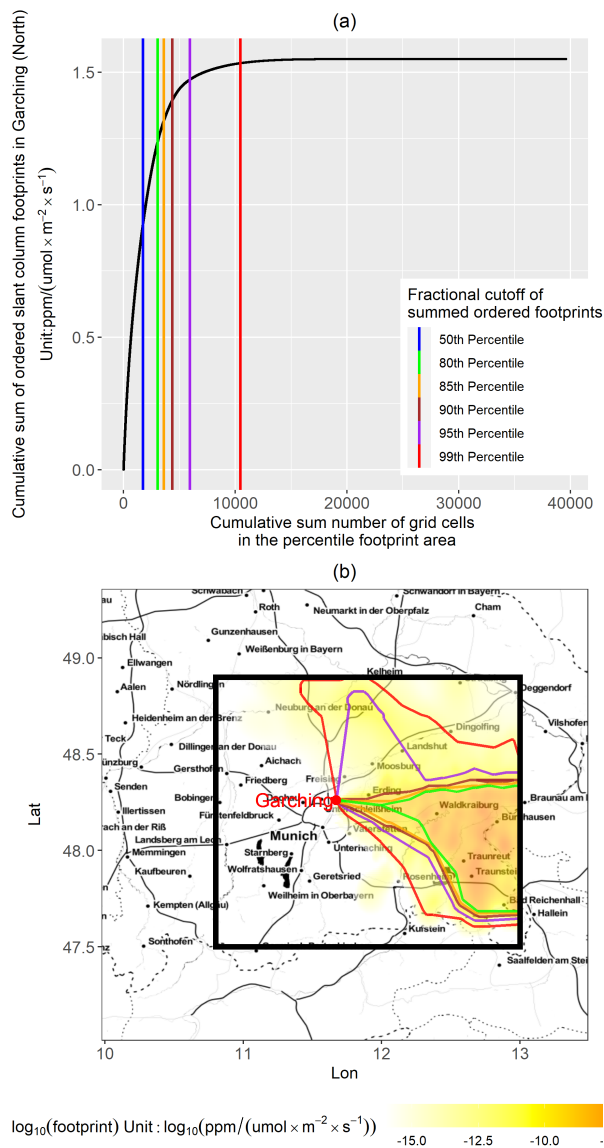
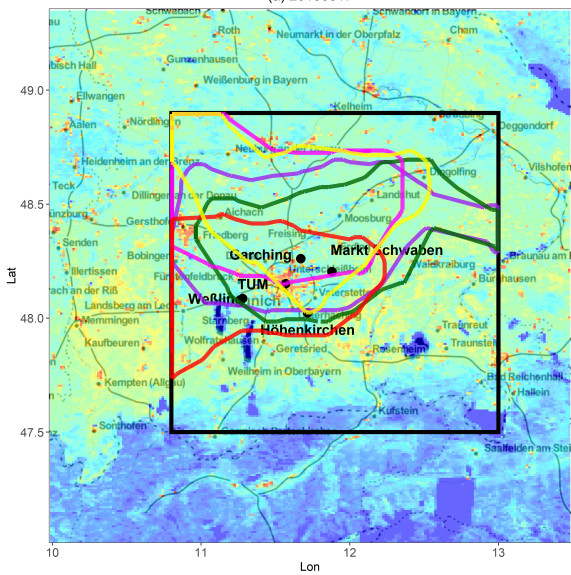


Figure S11. (a) The cumulative contribution of sorted slant column footprints to footprint area and concentration for one sample site and time: Garching at 11 am on 16 August, 2018 (trajectories running backwards for 10 hours). Six percentile thresholds were used for selecting points with footprints at or higher than threshold value. (b) The slant column footprint and its percentile contours: red for the 99th percentile, purple for the 95th percentile, brown for 90th percentile, orange for 85th percentile and green for 80th percentile. @ggmap (Kahle and Wickham, 2013)

Table S7. List of receptor times for our five measurement sites from 18 to 22 August, 2018.

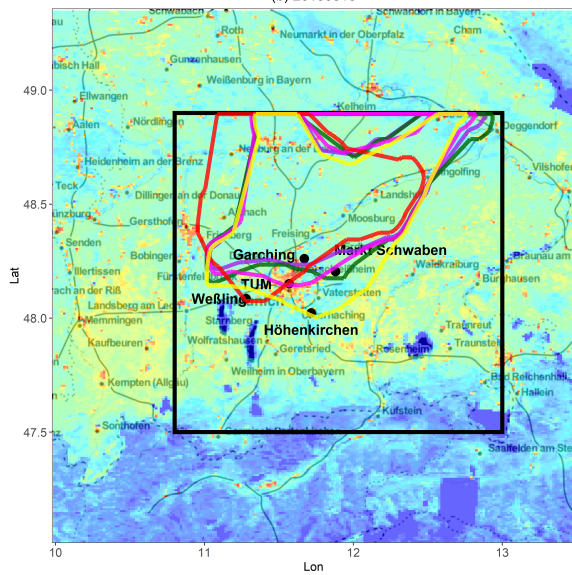
Date	Receptor time (UTC)				
	Garching (North)	Markt Schwaben (East)	TUM (Center)	Weßling (West)	Höhenkirchen (South)
20180816	11:00	11:00	12:00	14:00	11:30
20180817	11:00	11:00	13:00	11:00	15:00
20180818	11:00	11:00	12:00	14:00	11:00
20180819	11:00	12:00	11:00	15:00	11:30
20180820	13:00	13:00	12:00	9:00	13:00
20180821	10:30	11:00	12:00	14:30	-
20180822	13:00	11:00	12:00	15:30	-

(a) 20180817



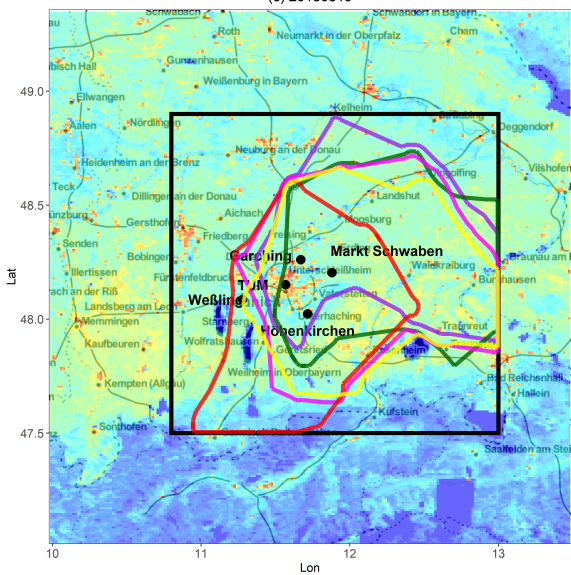
Emission fluxes of CH₄ (mol/(km² × hr))

(b) 20180818



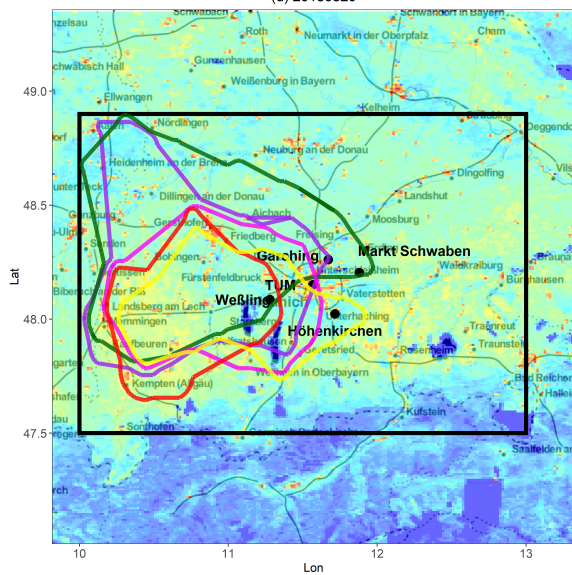
Emission fluxes of CH₄ (mol/(km² × hr))

(c) 20180819



Emission fluxes of CH₄ (mol/(km² × hr))

(d) 20180820



Emission fluxes of CH₄ (mol/(km² × hr))

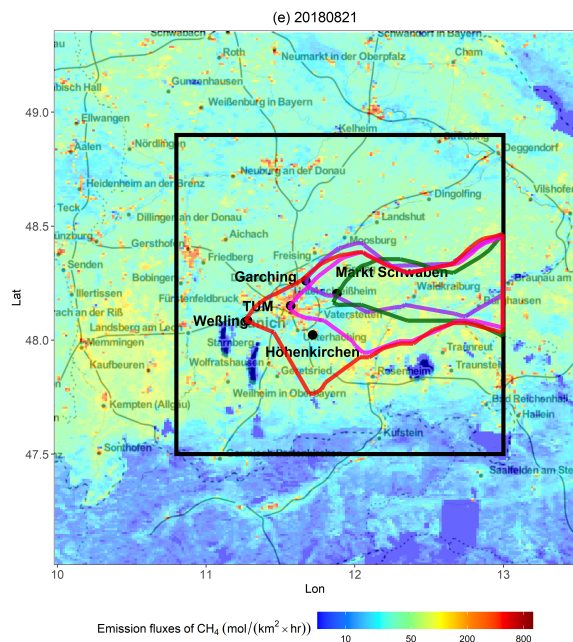


Figure S12. Footprint contours from 18 to 21 August at up- and downwind sites with different colors: red for Weßling (West), green for Markt Schwaben (East), purple for Garching (North) and pink for TUM (Center), yellow for Höhenkirchen (South). @ggmap (Kahle and Wickham, 2013)

S13 Time series of $\Delta XCH_{4,sla}^S$

In terms of $\Delta XCH_{4,sla}^S$, shown in Fig. S13, the modelled values generally show quite slight variations and are mostly positive during the day, while the measured concentration gradients between the down- and upwind sites are mainly negative. With NE/E winds, the instruments always measure strong signals at the upwind sites (i.e., Garching (north) and Markt Schwaben (east)) compared to the downwind sites, which cannot be reproduced by the model. As a large methane sink over the city is not expected, the most likely cause for this phenomenon is missing or underestimated emission sources located upstream of the upwind sites, located somewhere to the northeast or east of the Garching and Markt Schwaben stations. Likewise, in the case with W/NW winds, the negative measured concentration gradients between the three down- and one upwind sites are found with -1.89 ppb in daily means and the model fails to reproduce these signals. Again, the measured column concentrations at the upwind sites (i.e., Weßling) are generally higher than at the downwind sites. Especially in the morning of 20 August, a clear strong increase was captured at the upwind side (see Fig. S13). However, none of these features could be replicated by the model. We postulate the presence of an unknown or underestimated source of emissions located upstream of Weßling as the most likely explanation.

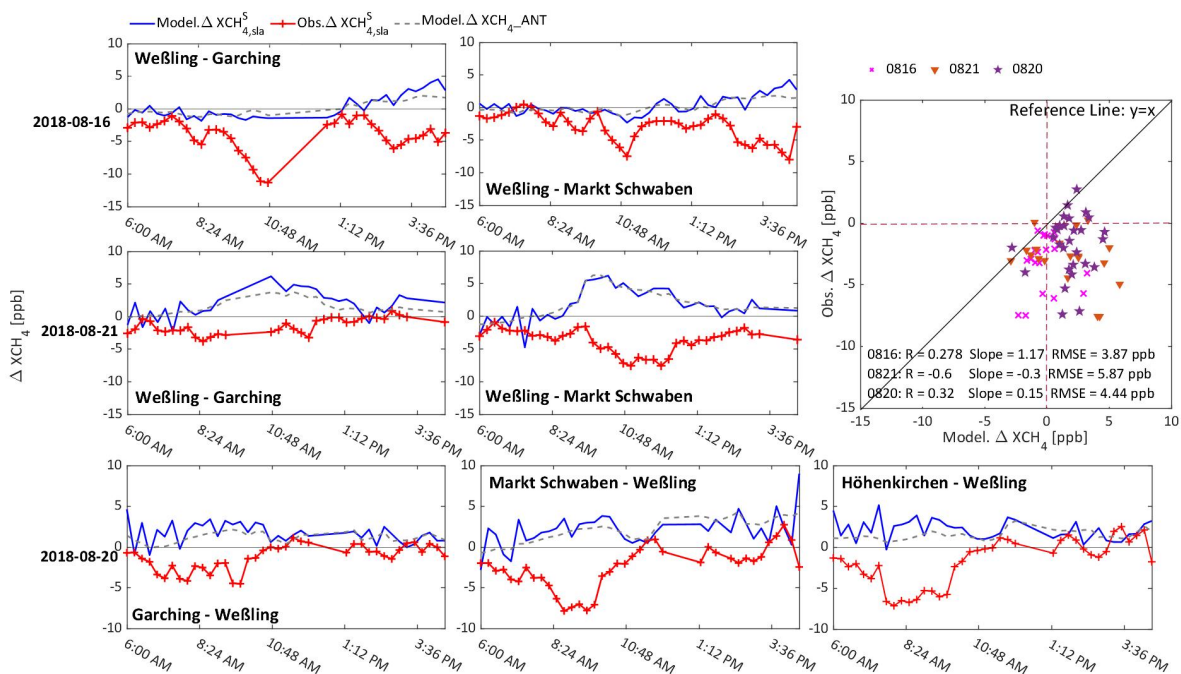


Figure S13. Time series of $\Delta XCH_{4,sla}^S$ for three targeted days and their scatter plot: 16 and 21 August with NE/E winds in the upper two rows, and 20 August with W/NW in the bottom line. The column concentration differences between the down- and the upwind sites are plotted as red solid lines for measurements, blue solid lines for the modelled full signal values, and grey dashed for the modelled contributions related to anthropogenic activities.

S14 Discussion of the CO₂ bias

In this study, we consider cases of CO₂ and CH₄ separately, as even though they are both simulated by the WRF and CAMS models, differences in their flux spatio-temporal patterns will lead to different biases when comparing to our measurements. The modelled total column concentration of CO₂ (XCO_2) is made up of three parts, the background contribution (Model.(X)CO₂_BCK, see Fig. S14), the enhancements induced by human activities (Model.(X)CO₂_ANT) and biogenic activities (Model.(X)CO₂_BIO). Each of these components could contribute to the model-measurement discrepancy. As discussed in the manuscript, the bias in the model-measurement comparison of XCO_2 could be attributed to three main causes: i) overestimation of the modelled background concentration from CAMS, ii) errors in concentration enhancements brought by anthropogenic fluxes, and iii) errors in simulated biogenic fluxes.

To understand the background-related cause in depth, we analyzed the variations and time series of CAMS itself, and compared the modelled and measured values. As seen from the red and orange curves in Fig. S14, the day-to-day magnitude and variations in Model. XCO_2 _BCK are mostly determined by its initialization (CAMS. XCO_2). For the simulations of background concentrations of tracer gas in WRF-Chem, it begins with initializing the 3-D field of the tagged tracer at the very beginning

of the simulation cycle (i.e. 30th July in our study) and it is updated via the lateral boundary conditions using global tracer fields at a 3-hour interval (using CAMS fields for both). On the basis of Model.XCO₂_BCK (orange), the daily-mean total column concentrations (green) vary slightly with the positive anthropogenic fluxes (Model.XCO₂_ANT) and the carbon sink from biogenic activities during the daytime (Model.XCO₂_BIO). The mean bias between CAMS.XCO₂ and Obs.XCO₂ (\pm its standard deviation) is 4.8 ± 0.7 ppm. Even though the overestimation of anthropogenic fluxes from the inventory and the uncertainty in the estimation of biogenic fluxes by the model could contribute to the model-measurement bias, this overestimation of CAMS overall plays a dominant role in the magnitude of the model-measurement bias of XCO₂. (Gałkowski et al., 2021; Tu et al., 2020) have supported this assumption that the CAMS (background) could cause a relatively large offset, rather than local emissions causing errors in excess of more than 3 ppm.

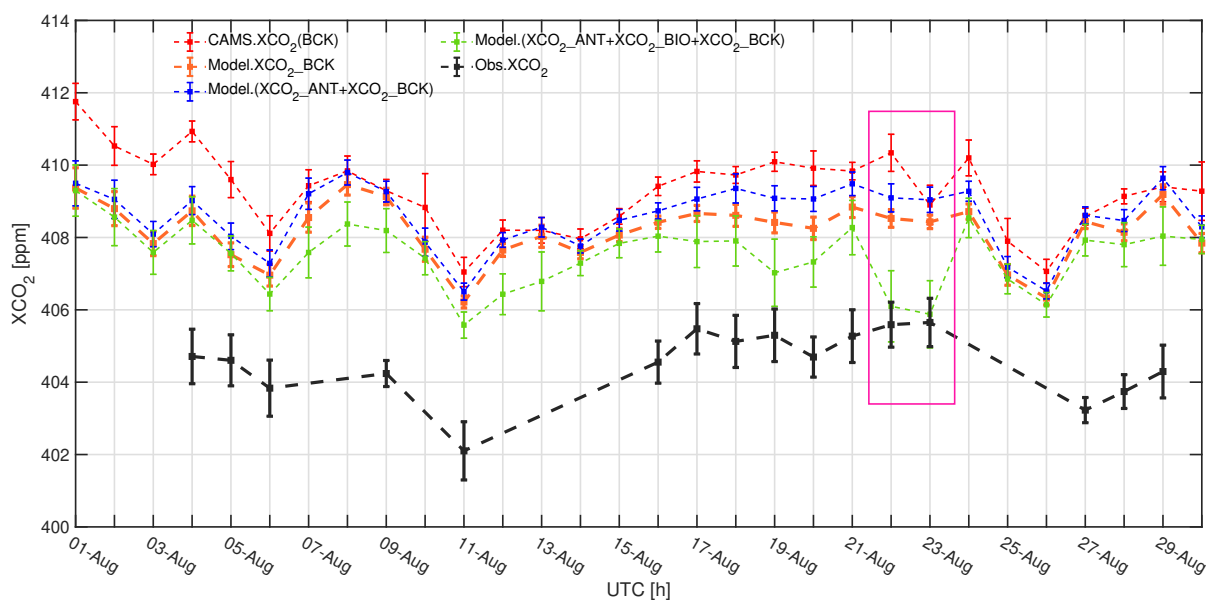


Figure S14. Time series of the daily mean measured values over five sites of MUCCNnet (black) and the averaged modeled XCO₂ from CAMS (red, CAMS.XCO₂_BCK) and WRF over D03 during the daytime (i.e., 6:00 UTC to 17:00 UTC). The modelled column concentrations are pressure-weighted means (see Eq. 1 in the manuscript). The error bars represent the standard deviation of the simulated values over D03 and over the five sites of MUCCNnet. The orange curve represents the mean modelled column background concentration (Model.XCO₂_BCK). The green curve shows the averaged total column concentration (Model.XCO₂_BCK+Model.XCO₂_ANT+Model.XCO₂_BIO) and the blue curve shows the averaged column concentrations considering only the background and anthropogenic activities (Model.XCO₂_BCK+Model.XCO₂_ANT), without biospheric fluxes.

The vertical distributions of the model values from CAMS and WRF-Chem have also been checked for 16, 17, and 22 August at 12 UTC (see Fig. S15). In general, the vertical distributions of CAMS CO₂ and Model CO₂_BCK are quite similar but slightly differ close to the ground level. This also indicates that the magnitudes and the vertical structure of background initialization of CO₂ (CAM.CO₂) play a decisive role in the modelled background (WRF.CO₂_BCK) and total concentrations.

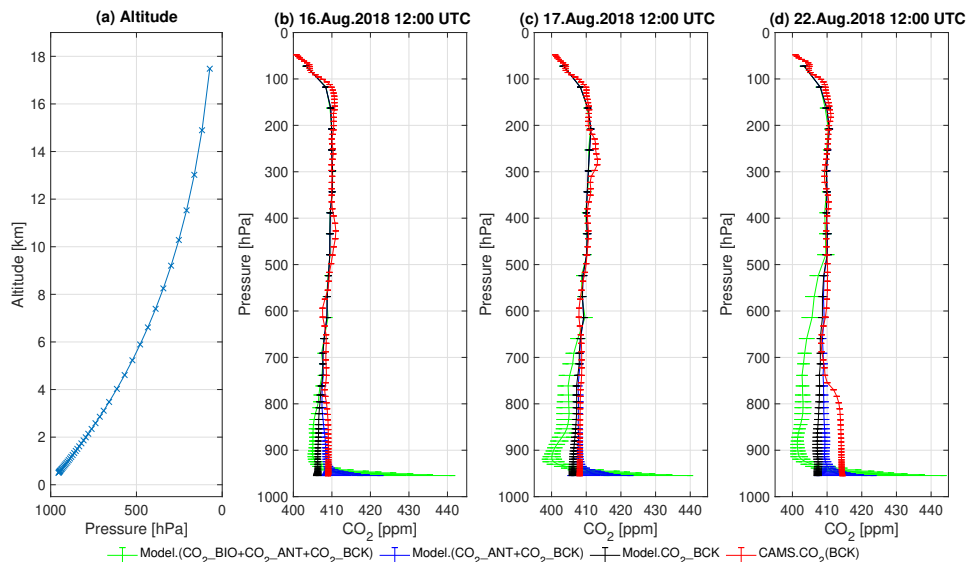


Figure S15. Vertical profiles of (a)Altitudes, averaged modelled CO_2 over D03 on (b)16, (c)17, and (d)22, August 2018 from CAMS and WRF-Chem. The red curve represents the values from CAMS, and the others stand for our model results, with green for the total values, blue for the sum of the background and the human-related enhancements, and red for the background.

Furthermore, emissions caused by human activities (blue, Fig. S15) contribute to the total concentration (green) within the planetary boundary layer (PBL, below approx. 2 km). For the enhancements associated with biogenic activities (green curve), carbon sources from respiration contribute significantly to the total concentration of CO_2 near ground level, while air masses heavily influenced by photosynthetic uptake (with less CO_2) and coming from the outer domain play a key role at higher altitude, especially on 22 August. This could explain the dip on this date (see the pink box in Fig. S14). The animation of biogenic concentrations over D01 attached in the supplement provides a visual perspective of this phenomenon.

Owing to the relatively large bias of CO_2 brought in by CAMS, we considered using the model-measurement MB over all the measurement dates (i.e., 3.7 ppm) to “correct” the modelled values. This could help to see if the model could reproduce similar variations to those seen by the measurements. These variations are determined by the modelled biogenic effects, initial emission fluxes from the inventory, the modelled advection of air masses influenced by human and biogenic fluxes, etc.

However, there is no significant model-measurement bias can be found in the daily-mean XCH_4 (cf. Fig. 3(c) & (d) of the main text). Due to the quite weak biogenic activities of CH_4 in and around Munich (cf. Fig. 5 of the main text), the model-measurement bias of CH_4 is mostly caused by the uncertainties in human-related emissions.

210 References

- Bieser, J., Aulinger, A., Matthias, V., Quante, M., and Van Der Gon, H. D.: Vertical emission profiles for Europe based on plume rise calculations, *Environmental Pollution*, 159, 2935–2946, <https://doi.org/10.1016/j.envpol.2011.04.030>, 2011.
- Brousse, O., Martilli, A., Foley, M., Mills, G., and Bechtel, B.: WUDAPT, an efficient land use producing data tool for mesoscale models? Integration of urban LCZ in WRF over Madrid, *Urban Climate*, 17, 116–134, <https://doi.org/10.1016/j.uclim.2016.04.001>, 2016.
- 215 Browne, P. A., de Rosnay, P., Zuo, H., Bennett, A., and Dawson, A.: Weakly coupled ocean–atmosphere data assimilation in the ECMWF NWP system, *Remote Sensing*, 11, 234, <https://doi.org/10.3390/rs11030234>, 2019.
- Collier, E., Mölg, T., Maussion, F., Scherer, D., Mayer, C., and Bush, A.: High-resolution interactive modelling of the mountain glacier–atmosphere interface: an application over the Karakoram, *The Cryosphere*, 7, 779–795, <https://doi.org/10.5194/tc-7-779-2013>, 2013.
- Dayalu, A., Munger, J. W., Wang, Y., Wofsy, S. C., Zhao, Y., Nehrkorn, T., Nielsen, C., McElroy, M. B., and Chang, R.: Evaluating China’s anthropogenic CO₂ emissions inventories: a northern China case study using continuous surface observations from 2005 to 2009, *Atmospheric Chemistry and Physics*, 20, 3569–3588, <https://doi.org/10.5194/acp-20-3569-2020>, 2020.
- 220 Demuzere, M., Bechtel, B., Middel, A., and Mills, G.: Mapping Europe into local climate zones, *PloS one*, 14, e0214474, <https://doi.org/10.1371/journal.pone.0214474>, 2019.
- Fasoli, B., Lin, J. C., Bowling, D. R., Mitchell, L., and Mendoza, D.: Simulating atmospheric tracer concentrations for spatially distributed receptors: updates to the Stochastic Time-Inverted Lagrangian Transport model’s R interface (STILT-R version 2), *Geoscientific Model Development*, 11, 2813–2824, <https://doi.org/10.5194/gmd-11-2813-2018>, 2018.
- 225 Friedl, M. A., Sulla-Menashe, D., Tan, B., Schneider, A., Ramankutty, N., Sibley, A., and Huang, X.: MODIS Collection 5 global land cover: Algorithm refinements and characterization of new datasets, *Remote sensing of Environment*, 114, 168–182, <https://doi.org/10.1016/j.rse.2009.08.016>, 2010.
- 230 Gaikowski, M., Jordan, A., Rothe, M., Marshall, J., Koch, F.-T., Chen, J., Agusti-Panareda, A., Fix, A., and Gerbig, C.: In situ observations of greenhouse gases over Europe during the CoMet 1.0 campaign aboard the HALO aircraft, *Atmospheric Measurement Techniques*, 14, 1525–1544, <https://doi.org/10.5194/amt-14-1525-2021>, 2021.
- Hase, F., Frey, M., Blumenstock, T., Groß, J., Kiel, M., Kohlhepp, R., Mengistu Tsidu, G., Schäfer, K., Sha, M., and Orphal, J.: Application of portable FTIR spectrometers for detecting greenhouse gas emissions of the major city Berlin, *Atmospheric Measurement Techniques*, 8, 3059–3068, <https://doi.org/10.5194/amt-8-3059-2015>, 2015.
- 235 Hersbach, H., Bell, B., Berrisford, P., Hirahara, S., Horányi, A., Muñoz-Sabater, J., Nicolas, J., Peubey, C., Radu, R., Schepers, D., et al.: The ERA5 global reanalysis, *Quarterly Journal of the Royal Meteorological Society*, 146, 1999–2049, <https://doi.org/10.1002/qj.3803>, 2020.
- Kahle, D. and Wickham, H.: ggmap: Spatial Visualization with ggplot2, *The R Journal*, 5, 144–161, <https://journal.r-project.org/archive/2013-1/kahle-wickham.pdf>, 2013.
- 240 Mahadevan, P., Wofsy, S. C., Matross, D. M., Xiao, X., Dunn, A. L., Lin, J. C., Gerbig, C., Munger, J. W., Chow, V. Y., and Gottlieb, E. W.: A satellite-based biosphere parameterization for net ecosystem CO₂ exchange: Vegetation Photosynthesis and Respiration Model (VPRM), *Global Biogeochemical Cycles*, 22, <https://doi.org/10.1029/2006GB002735>, 2008.
- Peckham, S. E., Grell, G. A., McKeen, S. A., Ahmadov, R., Barth, M., Pfister, G., Wiedinmyer, C., Fast, J. D., Gustafson, W. I., Ghan, S. J., Zaveri, R., Easter, R. C., Barnard, J., Chapman, E., Hewson, M., Schmitz, R., Salzmann, M., and Freitas, S. R.: WRF-Chem Version 3.9.1.1 User’s Guide, Tech. rep., National Center for Atmospheric Research, https://ruc.noaa.gov/wrf/wrf-chem/Users_guide.pdf, 2017.
- 245

- Pillai, D., Gerbig, C., Kretschmer, R., Beck, V., Karstens, U., Neininger, B., and Heimann, M.: Comparing Lagrangian and Eulerian models for CO₂ transport—a step towards Bayesian inverse modeling using WRF/STILT-VPRM, *Atmospheric Chemistry and Physics*, 12, 8979–8991, <https://doi.org/10.5194/acp-12-8979-2012>, 2012.
- 250 Rémy, S., Kipling, Z., Flemming, J., Boucher, O., Nabat, P., Michou, M., Bozzo, A., Ades, M., Huijnen, V., Benedetti, A., et al.: Description and evaluation of the troposphere aerosol scheme in the European Centre for Medium-Range Weather Forecasts (ECMWF) Integrated Forecasting System (IFS-AER, cycle 45R1), *Geoscientific Model Development*, 12, 4627–4659, <https://doi.org/10.5194/gmd-12-4627-2019>, 2019.
- See, L., Perger, C., Duerauer, M., Fritz, S., Bechtel, B., Ching, J., Alexander, P., Mills, G., Foley, M., O'Connor, M., et al.: Developing a community-based worldwide urban morphology and materials database (WUDAPT) using remote sensing and crowdsourcing for improved urban climate modelling, in: 2015 Joint Urban Remote Sensing Event (JURSE), pp. 1–4, IEEE, <https://doi.org/10.1109/JURSE.2015.7120501>, 2015.
- 255 Super, I., Dellaert, S. N., Visschedijk, A. J., and Denier van der Gon, H. A.: Uncertainty analysis of a European high-resolution emission inventory of CO₂ and CO to support inverse modelling and network design, *Atmospheric Chemistry and Physics*, 20, 1795–1816, <https://doi.org/10.5194/acp-20-1795-2020>, 2020.
- 260 Tu, Q., Hase, F., Blumenstock, T., Kivi, R., Heikkinen, P., Sha, M. K., Raffalski, U., Landgraf, J., Lorente, A., Borsdorff, T., Chen, H., Dietrich, F., and Chen, J.: Atmospheric CO₂ and CH₄ abundances on regional scales in boreal areas using Copernicus Atmosphere Monitoring Service (CAMS) analysis, Collaborative Carbon Column Observing Network (COCCON) spectrometers, and Sentinel-5 Precursor satellite observations, *Atmospheric Measurement Techniques*, 13, 4751–4771, <https://doi.org/amt-13-4751-2020>, 2020.
- Vogel, F. R., Frey, M., Staufer, J., Hase, F., Broquet, G., Xueref-Remy, I., Chevallier, F., Ciais, P., Sha, M. K., Chelin, P., et al.: XCO₂ in an emission hot-spot region: the COCCON Paris campaign 2015, *Atmospheric Chemistry and Physics*, 19, 3271–3285, <https://doi.org/10.5194/acp-19-3271-2019>, 2019.
- 265